Nanoscale

Accepted Manuscript

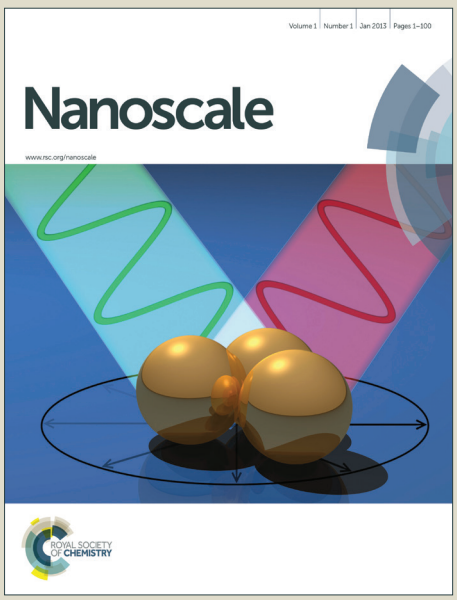

ROYAL SOCIETY OF CHEMISTRY

www.rsc.org/nanoscale

RSCPublishing

ARTICLE

Wet-spun, Porous, Orientational Graphene Hydrogel Films for High-performance Supercapacitor Electrodes

Cite this: DOI: 10.1039/x0xx00000x

Received 00th January 2012,
Accepted 00th January 2012

DOI: 10.1039/x0xx00000x

www.rsc.org/

Liang Kou,[a,b] Zheng Liu,[a] Tieqi Huang,[a] Bingna Zheng,[a] Zhanyuan Tian,[b] Zengshe Deng[b] and Chao Gao*[a]

Supercapacitors with porous electrodes of graphene macroscopic assembly are supposed to have high energy storage capacity. However, a great number of the "close pores" in porous graphene electrodes are invalid because electrolyte ions cannot infiltrate. How to fast prepare porous graphene electrodes with reduced "close pores" is essential for higher energy storage. Here we proposed a wet-spinning assembly approach based on the liquid crystal behavior of graphene oxide to continuously spin orientational graphene hydrogel film with “open pores”, which are used directly as binder-free supercapacitor electrodes. The resultant supercapacitor electrodes show better electrochemical performance than those with disordered graphene sheets. Furthermore, three reduction methods including hydrothermal treatment, hydrazine and hydroiodic acid reduction are used to evaluate the specific capacitances of graphene hydrogel film. Hydrazine-reduced graphene hydrogel film shows highest capacitance of 203 F/g at 1 A/g and maintains 67.1% specific capacitances (140 F/g) at 50 A/g. The combination of scalable wet-spinning technology and orientational structure makes graphene hydrogel films an ideal electrode material for supercapacitors

Introduction

Supercapacitors are widely considered as a crucial kind of energy storage devices due to their high power density, long cycle life, fast charge-discharge rate, improved safety, along with the potential relatively high energy density closed to batteries. [1-4] The superior properties of graphene such as ultrahigh specific area, excellent electrical conductivity and chemical stability make it an ideal candidate for constructing electrodes of supercapacitors.[5-9] Compared with supercapacitor electrodes made from graphene powder with binder, the electrodes using binder-free macroscopic assembled graphene reduce the volume and weight of the supercapacitors, without compromising of electrical conductivity of the electrodes, essential for the fast current response.[10-12] To acquire binder-free supercapacitors with high capacitance, the electrodes of macroscopic assembled graphene must be made into porous structures to assure the high ion-accessible area.[13-18]

Template and template-free methods are two main approaches to acquire porous macroscopic assembled graphene. For template methods, graphene or graphene oxide (GO) nanosheets were firstly deposited on templates such as nickel foams,[19-21] polystyrene balls,[22,23] silica balls,[24] followed by etching/dissolving the templates using acids or organic solvents. These methods always involve more steps, thus they are time-consuming and costly. For template-free methods, they include hydrothermal reduction of GO dispersion,[7,25,26] freeze-drying aqueous solutions of graphene,[27] autoclaved leavening and steaming of GO layered films,[28] electrochemical deposition of GO onto the electrode surfaces.[29,30] However, these methods are hard to be scaled up due to the limitation of apparatus and the change of inner pore structure within the bulk mass. Besides, porous macroscopic assembled graphene constructed by these methods are generally arranged without orientation, which leads to many ion-blocking “close pores” and thus lowers the electrochemical performance of supercapacitors.[31] Hence, how to fast , efficiently, mass produce porous macroscopic assembled graphene with orientational graphene wall at low cost is an urgent challenge to be addressed.

Here, inspired by the wet-spinning technology we proposed to spin GO fibers or films based on the liquid crystal (LC) behavior of GO aqueous solution,[32-35] we developed a novel wet-spinning assembly approach by using a geometric confined line-shape flat nozzle to continuously obtain GO hydrogel films (GOHF). Because of the LC behavior of GO and further orientation during the wet-spinning process, both the as-prepared porous GOHF and the resultant reduced GOHF (GHF) are highly orientational with GO or graphene nanosheets arraying vertically to cross section of films. The hydrothermally reduced GHF electrodes have capacitances of 183 F/g at the current density of 1 A/g, much higher than that (111 F/g) of electrodes with disordered graphene sheets using the same reduction method. Besides, due to the microstructure difference of GHF caused by the reduction methods used, hydrazine-reduced GHF (GHF-HZ) electrodes exhibits the best capacitance (203 F/g at 1 A/g) and rate capability compared with hydrothermally reduced GHF (GHF-HT) electrodes and hydroiodic acid-reduced GHF (GHF-HI) electrodes.

Experimental section

Preparation of orientational GHF: Typically, GO dispersion (10.0 mg/mL) prepared according to our previous papers[27,36,37] was injected into the coagulation bath (5 wt% $CaCl_2$, $V_{ethanol}/V_{water}$ = 1 : 5) at a spinning rate of 0.5 μL/min using a home-made runner with a rectangular cross section (Figure S1). The as-spun GO gel films were then collected and pulled out by PET substrate film. GHF-HT was prepared by placing GO gel films into Teflon-lined autoclave and maintained at 180 ℃ for 18 h. GHF-HZ and GHF-HI were obtained by placing GO gel films into sealed glass Petri dishes with 0.5 wt% hydrazine aqueous solution and 0.5 wt% hydroiodic acid aqueous solution, respectively, and then heated at 95 ℃ for 3 h.

Preparation of disordered GHC-HT: GHC-HT was prepared according to previous publications.[7,23] A 20 mL 10 mg/mL GO aqueous dispersion was sealed in a 50-mL Teflon-lined autoclave and maintained at 180 ℃ for 18 h. Then the autoclave was naturally cooled to room temperature and GHC-HT was obtained.

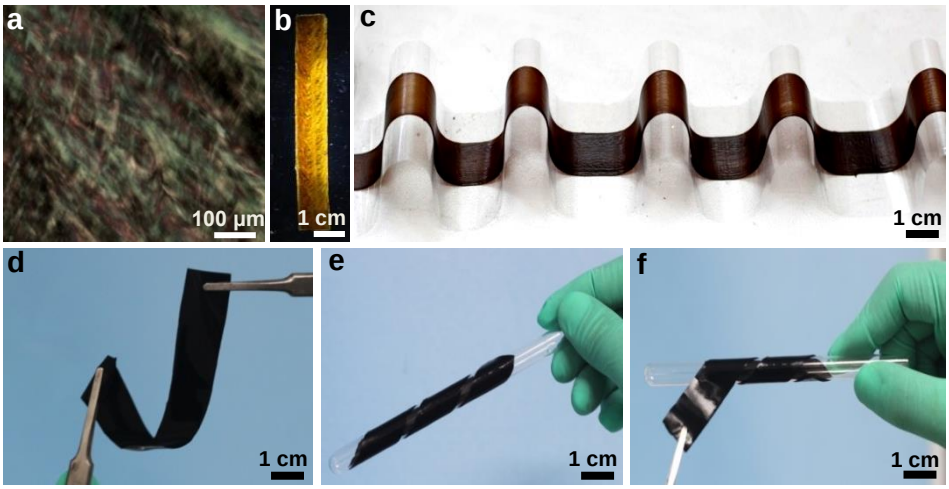

Figure 1. (a) POM image of GO liquid crystal aqueous dispersion (10 mg/mL). (b) Image of a GO gel film between crossed polarizers. (c) Image of 1 meter-long GOHF with PET substrate. (d-f) Images of flexible, free-standing GHF.

Assembly of Supercapacitors and Electrochemical Measurements: For electrochemical tests, binder-free GHF based supercapacitors were assembled in a two electrode system. GHFs were cut into circular sheets with diameters of 10 mm and immersed in 1 M H_2SO_4. They were then placed in Constant Temperature Vibrator to vibrate at a speed of 100 rpm for 24 h at 35 ℃ to make H_2SO_4 electrolyte penetrate into the inner of GHFs. Using platinum sheets as current collectors, cellulose ester films of 0.22 μm pores, 1 M H_2SO_4 as aqueous electrolyte solution, we carried out the electrochemical tests by employing an apparatus shown in Figure S2.

Apparatus for characterizations: Scanning electron microscope (SEM) images were taken on a Hitachi S4800 field-emission SEM system. Polarized-light optical microscopy (POM) observations were performed with a Nikon E600POL. Cyclic voltammetry (CV), electrochemical impedance spectroscopy (EIS) and galvanostatic charge-discharge (GCD) measurements were performed using an electrochemical workstation (CHI 660e, CH Instruments, Inc.). The tensile stress-strain tests were performed on a Microcomputer Control Electronic Universal Testing Machine made by REGER in China (RGWT-4000-20). Thermogravimetric analysis (TGA) was carried out on a Perkin-Elmer Pyris 6 TGA instrument under nitrogen with a heating rate of 10 ℃/min. X-ray Diffraction (XRD) was carried out in X'Pert PRO diffractometer equipped with Cu Kα radiation (40 kV, 40 mA). X-ray photoelectron spectroscopy (XPS) were performed with a RBD upgraded PHI-5000C ESCA system (Perkin-Elmer) with Mg Kα radiation (hν = 1 253.6 eV) at a power of 250 W.

Results and discussion

The schematic diagram for fabricating GOHF and the photograph of line-shape flat nozzle are shown in Figure S1. GO solution is injected to the line-shape flat nozzle and flows out into coagulation bath to form GOHF, which is then pulled out by PET substrate connected by a roller. It is well-recognized that GO solutions can form LC because of their high aspect ratio (or width/thickness ratio) and sufficient dispersibility/solubility,[32-34] as evidenced by POM observation (Figure 1a). After the shear flow induced orientation and subsequent coagulation, GO solution was assembled into GOHF. The polarized optical photo of GOHF between two crossed polarizers exhibits golden yellow fibriform LC textures along the flow direction (Figure 1b), implying that GO nanosheets were assembled into highly orientational GO LC domains parallel to the flow direction. Owing to the advantage of continuous preparation for wet-spinning technology, 1 meter-long, uniform GOHF with PET substrate was readily prepared, which is flexible enough to be bended as multi-saddle shape (Figure 1c). After reduction, GHF-HT, GHF-HZ and GHF-HI have conductivities of 0.7, 32.2, 333 S/m and contain about 98.85, 99.33 and 98.31 wt% water, respectively. The as-prepared free-standing GHFs (Figure 1d) are flexible and robust (Figure S3, mechanical strength (σ) 0.56 MPa, elongation at break (ε) 56.76 % for GHF-HT, σ 0.40 MPa, ε 125.42 % for GHF-HZ, σ 0.25 MPa, ε 65.22 % for GHF-HI), and they can wrap and unwrap on the glass rod without any crack (Figure 1e, f). The cross sectional microstructure of freezing-dried GHF-HT in Figure 2 a-c shows that hydrogel film with uniform thickness of *ca.* 50 μm is made of orientational graphene nanosheets vertical to the cross section. Pores formed by orientational graphene nanosheets walls with a certain dislocation are distributed evenly over the whole hydrogel film. The graphene nanosheets walls are extremely thin (below 10 nm) observed from the magnified SEM image (Figure 2 c), containing only few layer of graphene nanosheets since the thickness of reduced GO is 0.4-0.8 nm.[27,38,39] The top views of

freezing-dried GHF-HT show that ductile, wrinkled graphene nanosheets are all tiled along the surface of GHF-HT (Figure 2 d-f), further testifying the orientation array of graphene sheets vertical to the cross section. An elliptical 2D pattern of small-angle X-ray scattering (SAXS) also indicates the sole orientational order of graphene nanosheets in GHF-HT (inset of Figure 2 f).[32,34]

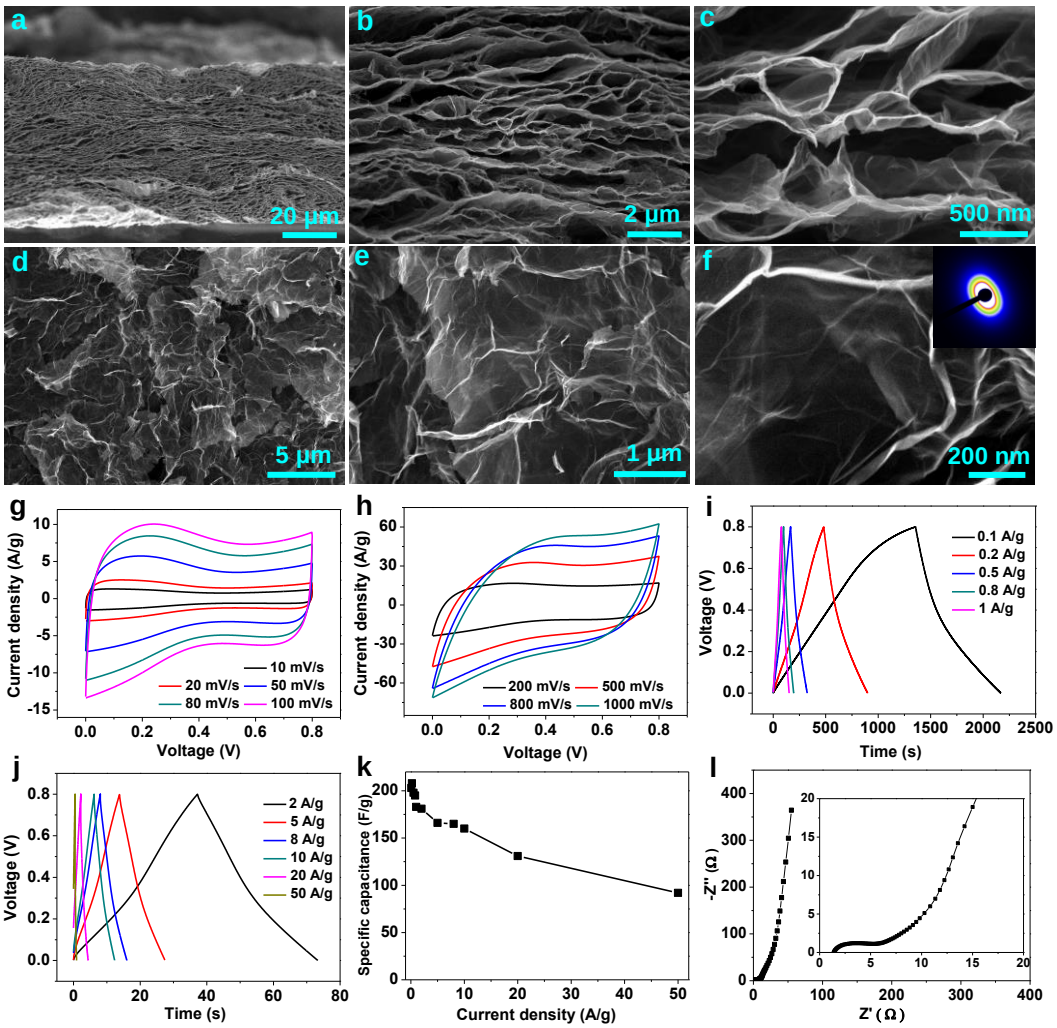

Figure 2. Side (a-c) and top (d-f) view SEM images of GHF-HT under different magnification, inset of f shows the 2D SAXS pattern of GHF-HT. CV curves of GHF-HT with scan rate of 10-100 mV/s (g) and 200-1000 mV/s (h). GCD curves of GHF-HT with charge/discharge current density of 0.1-1 A/g (i) and 2-50 A/g (j). (k) The calculated specific capacitances of GHF-HT with charge/discharge current density ranging from 0.1 A/g to 50 A/g. (l) Nyquist plot of GHF-HT, inset shows the magnified high-frequency regions.

The orientational, porous structure combined with satisfying electrical conductivity makes GHF-HT as an ideal candidate of binder-free supercapacitor electrodes, so we assembled GHF-HT into two-electrode symmetrical supercapacitors. Their electrochemical performances were evaluated by CV, GCD, and EIS tests. CV curves at low scan rate of 10-100 mV/s resemble rectangle (Figure 2 g), demonstrating that GHF-HT possesses both electrochemical double layer capacitance (EDLC) and faradaic pseudocapacitance. Faradaic pseudocapacitance comes from the residual oxygen-containing groups after hydrothermal reduction,[40] which can be proved by 13% thermal weight loss from thermal gravity analysis (TGA) (Figure S4). The rectangular shape of CV curves at high scan rate of from 200 to 1000 mV/s maintains well (Figure 2 h), indicating the short ion transport distance resulted from unobstructed ion channels.[7] The specific capacitances of GHF-HT electrodes calculated from GCD curves (Figure 2 i, j) at different current densities are shown in Figure 2 k. GHF-HT electrode shows a very high capacitance value and good rate capability. At a current density of 0.2 A/g, the specific capacitance is 208 F/g (33.3 F/cm^3) and declined to 183 F/g (29.3 F/cm^3) at 1 A/g. Even at 10 A/g, this binder-free supercapacitor electrode shows high specific capacitance of 160 F/g, comparable to that of electrodes using graphene powder with record specific surface area 3100 m^2/g.[41] Nyquist plots (Figure 2 l) of GHF-HT based supercapacitor is characterized by a humble arc in the high frequency region. It is related to the electronic transport within electrodes, between electrodes and electrolyte, electrodes and current collectors, and the x axis intercept of plot shows a small equivalent series resistance (1.3 Ω). A relatively short 45^o Warburg region in the middle frequency reflects that GHF-HT has a porous structure as confirmed by SEM images.[42] A vertical line in the low frequency region indicates a pure capacitive behavior. Since the thickness of GHF-HT can be readily tuned by changing the concentration of spinning dope or nozzle thickness, we also prepared GHF-HT with thickness of 5 and 25 μm. The electrochemical

properties of GHF-HT with different thickness were then investigated. The results show that the thickness of GHF-HT below 50 μm has no effect on the specific capacitances and rate capabilities of GHF-HT based supercapacitors.

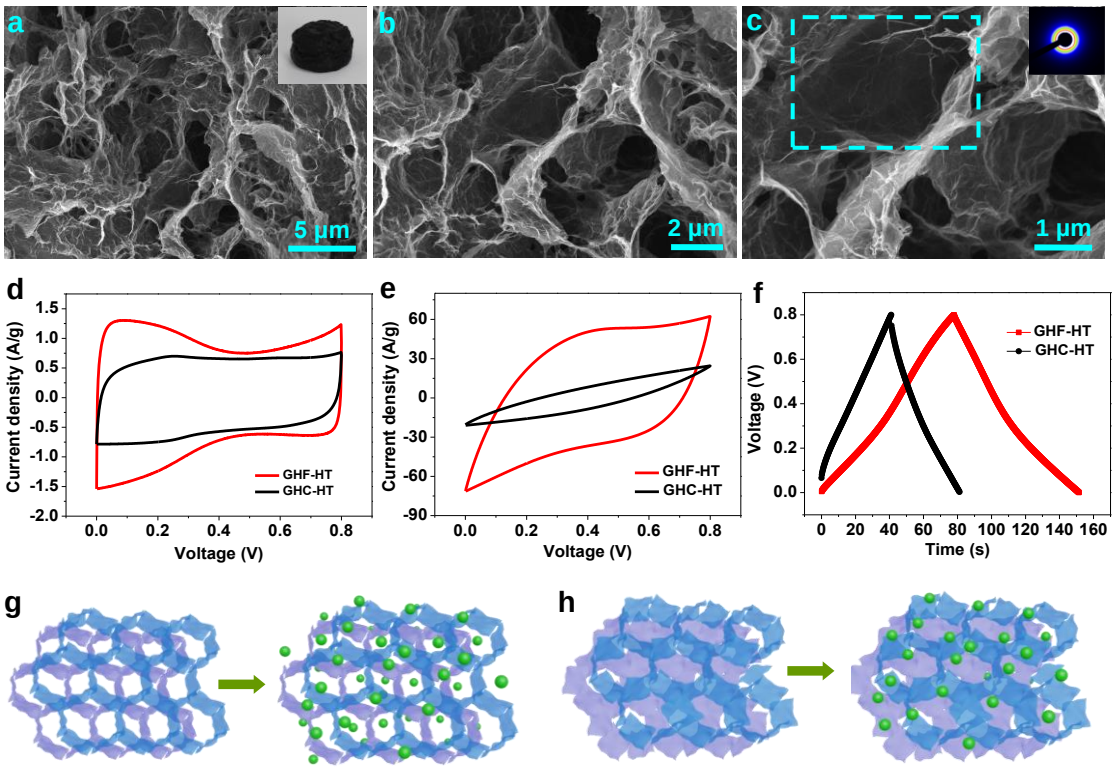

Figure 3. (a-c) SEM images of GHC-HT under different magnification, inset of a shows the digital photo of GHC-HT, inset of c shows the 2D SAXS pattern of GHC-HT. CV curves of GHF-HT and GHC-HT at scan rate of 10 (d) and 1000 (e) mV/s. (f) GCD curves of GHF-HT and GHC-HT at 1 A/g. (g) Schematic illustration of orientated GHF-HT facilitating ion transport. (h) Schematic illustration of disordered GHC-HT blocking ion penetration.

For comparison, graphene hydrogel cylinder (inset of Figure 3 a) prepared by hydrothermal treatment of GO solution (GHC-HT)[25,42] was also employed as control supercapacitor electrodes to demonstrate the advantage of orientational structure of GHF-HT. Hydrophobic and π-π interactions along with the residual oxygenated functional groups on the graphene sheets caused a 3D random stacking between flexible graphene sheets for GHC-HT.[25] As shown in Figure 3 a-c, the inner structure of GHC-HT is disorderly and some pores are plugged by adjacent graphene sheets (rectangular area in Figure 3 c). The 2D SAXS pattern also indicates that GHC-HT has no orientation (inset of Figure 3 c). The as-prepared GHC-HT is then cut into slices with a knife, and used as electrodes of supercapacitors. At low scan rate of 10 mV/s, the area circled by CV curve is obviously smaller than that for GHF-HT based supercapacitor (Figure 3 d). At high scan rate of 1000 mV/s, CV curve of GHC-HT based supercapacitor is transformed to fusiform, while it keeps relatively well for GHF-HT based supercapacitor (Figure 3 e). Calculated from GCD curves (Figure 3 f), the specific capacitances of GHC-HT and GHF-HT are 111 and 183 F/g at the current density of 1 A/g, respectively. Since GO stock and reduction condition are identical for GHC-HT and GHF-HT, the difference of specific capacitances can be only caused by the orientational array of graphene nanosheets. As illustrated in Figure 3 g, GHF-HT with orientational graphene nanosheets allows electrolyte to penetrate into the inner part of electrode and touch more graphene nanosheets, responsible for the higher specific capacitances and better rate capability. On the contrary, disordered graphene wall constructed GHC-HT has many pores blocked by other graphene walls (Figure 3 h), which not only increases the volume of the electrodes and the ion transport distance, but also largely reduces the electrolyte-accessible area, leading to relatively lower specific capacitances and rate capability. Therefore, our wet-spun GHF-HT with orientational graphene nanosheets is much more competitive than GHC-HT with disorder graphene nanosheets in the application of binder-free supercapacitor electrodes.

Besides GHF-HT, GHF-HZ and GHF-HI were also used as supercapacitor electrodes to estimate the effect of reduction methods on electrochemical performance. The microscopic morphologies of GHF-HZ (Figure 4 a-c) and GHF-HI (Figure 4 d-f) are similar to GHF-HT with graphene sheets vertical to cross section of the hydrogel films, proved by both side and top views of SEM images. The elliptical 2D patterns of SAXS also demonstrate the orientational structure of GHF-HZ (inset of Figure 4 c) and GHF-HI (inset of Figure 4 f). Compared with GHF-HT, the CV curves of GHF-HZ and GHF-HI at the low scan rate of 10 mV/s are much more like a rectangle because of the less oxygen-containing groups after chemical reduction (Figure S4, weight loss at ca. 200°C). The GHF-HI based supercapacitor shows the smallest area circled by CV curves, which indicates the lowest specific capacitance. At high scan rate of 1000 mV/s, the shapes of CV curves of GHF-HT and GHF-

HZ are kept well, while it deformed seriously for GHF-HI based supercapacitor, indicating its relatively poor ion transportation.

GCD curves of GHF-HT, GHF-HZ and GHF-HI can retain nearly linear and symmetric charge/discharge profiles at the current density of 1 A/g (Figure 4 i). Due to the lowest electrical conductivity among three GHFs, GHF-HT exhibits the highest potential drops when the current density increases to 50 A/g (Figure 4 j). The rate capabilities of these GHF electrodes are summarized in Figure 4 k. The specific capacitances for GHF-HT, GHF-HZ and GHF-HI are 208, 211 and 117 F/g (33.3, 33.7 and 18.7 F/cm^3) at 0.2 A/g, respectively, and maintained 88.0%, 96.2%, 91.4% at 1 A/g. As the current density increased to 50 A/g, GHF-HT, GHF-HZ and GHF-HI electrodes maintain their 44.2%, 67.1%, 29.9% specific capacitances. Apparently, GHF-HZ electrode presents better electrochemical performance in both specific capacitance and rate capability. Nyquist plot also indicates that GHF-HZ is a more suitable electrode material of supercapacitor since it has lower equivalent series resistance (1.31 Ω), shorter Warburg impedance and more vertical curve at low frequency (Figure 4 l). Table S1 summerizes the comparison data of our GHF-HZ supercapacitors with supercapacitors using graphene hydrogel electrodes reported previously, confirming the superior electrochemical performance of GHF-HZ.

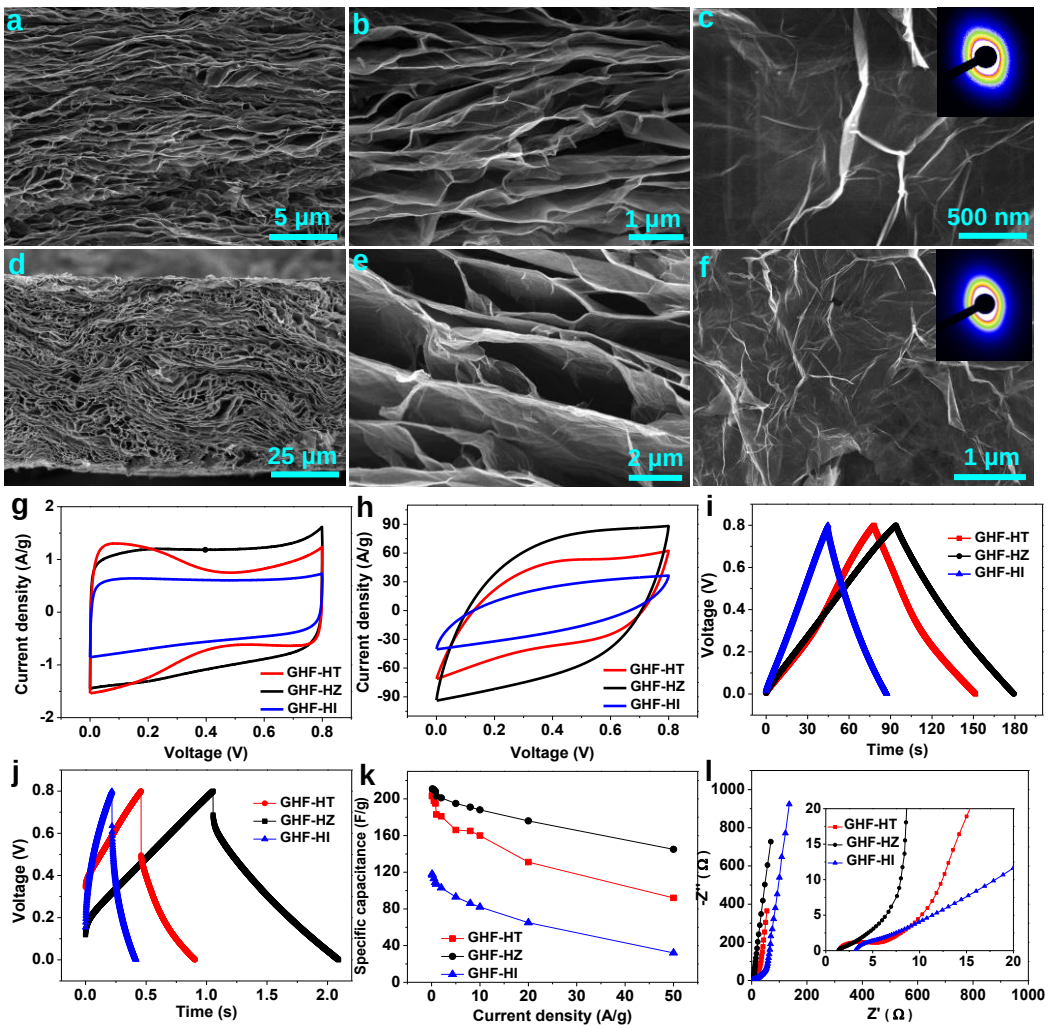

Figure 4. Top (a, b) and side (c) view of SEM images of GHF-HZ, inset of c shows 2D SAXS pattern of GHF-HZ. Top (d, e) and side (f) view of SEM images of GHF-HI, inset of f shows 2D SAXS pattern of GHF-HT. CV curves of GHF-HT, GHF-HZ and GHF-HI at 10 mV/s (g) and 1 V/s (h), respectively. GCD curves of GHF-HT, GHF-HZ and GHF-HI at 1 (i) and 50 A/g (j). Rate capability (k) and Nyquist spots (l) of these three GHF based supercapacitors.

The superior electrochemical performance of GHF-HZ is possibly attributed to the following two factors: N heteroatom introduction and higher specific area. For GHF-HZ electrodes materials, the introduction of 4.67% N heteroatoms (Figure 5 a) not only increases their wettability,[43] but also endows them with faradaic pseudocapacitance.[40,43] Moreover, GHF-HZ shows higher specific area of 146 m^2/g than that of GHF-HT (102 m^2/g) and GHF-HI (84 m^2/g), which leads to the highest specific capacitance among three GHFs. (NOTE: the low specific area values are derived from freeze-drying process,[44] and macropores of our GHFs exceed the test range[45]) The reason for the specific area difference of GHF electrodes coming from the identical GO gel films can be deduced from the corresponding XRD data. As shown in Figure 5 b, GHF-HZ shows a wide diffraction peak, corresponding to a grain size of 0.901 nm calculated from Scherrer formula (D = Kλ/Bcosθ, where D stands for grain size, K is Scherrer constant of 0.89, λ is X ray wavelength of 0.154 nm, B represents the full width at half maximum, θ is diffraction angle). GHF-HT and GHF-HI exhibit relatively narrow diffraction peaks related to grain sizes of 1.463 and 2.509 nm. The biggest grain size of GHF-HI indicates the highest

reduction extent and the most restored sp2 area of graphene sheets, which leads to severest π-π restacking and smallest specific area. For GHF-HZ, the introduction of N heteroatoms combined with gas release during the reduction process destroys the restacking of graphene sheets, resulting in the smallest grain size and highest specific area.[46] Long cycle life of supercapacitors is important for their practical applications.[36] The cycle lives of these three GHFs based supercapacitors were tested between 0 and 0.8 V at current density of 1 A/g. As shown in Figure 5 c, the specific capacitance of GHF-HZ electrodes has almost no change (99.72% of its initial value of 203 F/g) after 10000 charge/discharge cycles. GHF-HT and GHF-HI also perform excellent cycle stability with cycle retention of 96.66% and 94.06%, reflecting an excellent electrochemical stability of GHF electrodes and a high degree of reversibility in the repetitive charge/discharge cycling tests. We further used the tandem device connected by three GHF-HZ based supercapacitor units in series to light up a light-emitting-diode (LED) lamp (Figure 5 d), demonstrating the potential application of this GHF based supercapacitors.

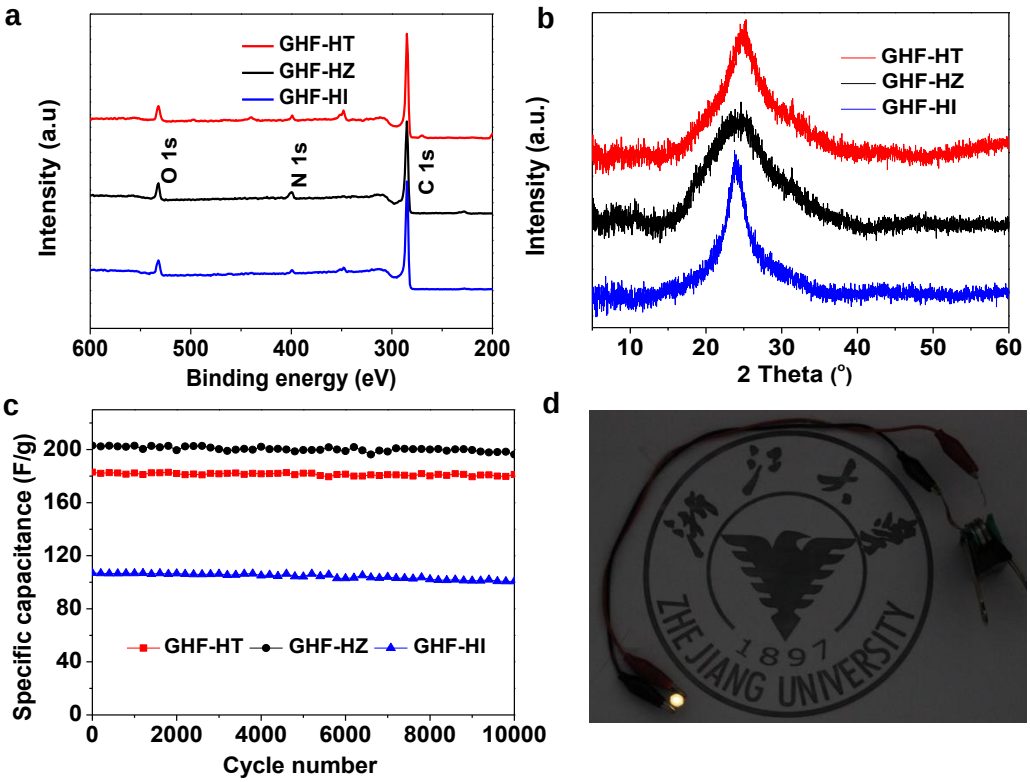

Figure 5. XRD (a), XPS (b) of GHF-HT, GHF-HZ and GHF-HI. (c) Cycling stability of GHF based supercapacitors at 1 A/g. (d) Photograph of a LED lamp powered by three supercapacitors assembled in series.

Conclusions

We proposed and demonstrated a wet-spinning assembly strategy to continuously prepare highly orientational graphene oxide hydrogel films. Graphene hydrogel films are then obtained by three different reduction methods. Using graphene hydrogel films as binder-free electrodes, we found that the orientational array of graphene nanosheets is beneficial to the penetration of electrolyte, which is responsible for the higher specific capacitance and better rate capability compared to porous graphene networks with disordered graphene nanosheets. In addition, graphene hydrogel films reduced by hydrazine exhibit the highest specific capacitance and best rate capability because of the smallest grain size, biggest specific area, along with the faradaic pseudocapacitance. The realization of large-scale production of hydrazine-reduced graphene hydrogel films with orientational graphene nanosheets paves the way for the next generation of high-performance supercapacitors.

Acknowledgements

This work is supported by the National Natural Science Foundation of China (no. 51173162 and no. 21325417), and Fundamental Research Funds for the Central Universities (no. 2013XZZX003).

Notes and references

[a] MOE Key Laboratory of Macromolecular Synthesis and Functionalization, Department of Polymer Science and Engineering, Zhejiang University, 38 Zheda Road, Hangzhou 310027, PR China. Tel: +86-(0)571-87952088
E-mail: chaogao@zju.edu.cn, cgao18@163.com
[b] Shaanxi Coal and Chemical Technology Institute Co., Ltd, 2 Jinye Road 1, Xi'an 710070, PR China.
Electronic Supplementary Information (ESI) available: [The schematic diagram for fabricating graphene oxide hydrogel film, stress-strain curves and TGA curves of three GHFs, digital photo of the test device for two-electrode system, comparison of electrochemical performance of our GHF-HZ supercapacitors]. See DOI: 10.1039/b000000x/

1 Simon, P.; Gogotsi, Y. *Nat. Mater*. **2008**, *7*, 845-854.
2 Wang, G.; Zhang, L.; Zhang, J. *Chem. Soc. Rev.* **2012**, *41*, 797-828.
3 Hall, P. J.; Mirzaeian, M.; Fletcher, S. I.; Sillars, F. B.; Rennie, A. J. R.; Shitta-Bey, G. O.; Wilson, G.; Cruden, A.; Carter, R. *Energ. Environ. Sci*. **2010**, *3*, 1238-1251.
4 Yang, X.; Cheng, C.; Wang, Y.; Qiu, L.; Li, D. *Science* **2013**, *341*, 534-537.
5 Nyholm, L.; Nyström, G.; Mihranyan, A.; Strømme, M. *Adv. Mater*. **2011**, *23*, 3751-3769.
6 Huang, Y.; Liang, J.; Chen, Y. *Small* **2012**, *8*, 1805-1834.
7 Chen, J.; Li, C.; Shi, G. *J. Phys. Chem. Lett*. **2013**, *4*, 1244-1253.
8 Zhu, Y.; Murali, S.; Cai, W.; Li, X.; Suk, J. W.; Potts, J. R.; Ruoff, R. S. *Adv. Mater*. **2010**, *22*, 3906-3924.
9 Zang, X.; Chen, Q.; Li, P.; He, Y.; Li, X.; Zhu, M.; Li, X.; Wang, K.; Zhong, M.; Wu, D.; Zhu, H. *Small* **2014**, *10*, 2583-2588.
10 Zhang, L. L.; Zhao, X.; Stoller, M. D.; Zhu, Y.; Ji, H.; Murali, S.; Wu, Y.; Perales, S.; Clevenger, B.; Ruoff, R. S. *Nano Lett.* **2012**, *12*, 1806-1812.
11 Cheng, Y.; Lu, S.; Zhang, H.; Varanasi, C. V.; Liu, J. Nano Lett. **2012**, *12*, 4206-4211.
12 Seo, D. H.; Han, Z. J.; Kumar, S.; Ostrikov, K. Adv. Energ. Mater. **2013**, *3*, 1316-1323.
13 Dong, X.-C.; Xu, H.; Wang, X.-W.; Huang, Y.-X.; Chan-Park, M. B.; Zhang, H.; Wang, L.-H.; Huang, W.; Chen, P. *ACS Nano* **2012**, *6*, 3206-3213.
14 Xu, Y.; Lin, Z.; Huang, X.; Liu, Y.; Huang, Y.; Duan, X. *ACS Nano* **2013**, *7*, 4042-4049.
15 Zhao, Y.; Hu, C.; Hu, Y.; Cheng, H.; Shi, G.; Qu, L. *Angew. Chem., Int. Ed*. **2012**, *51*, 11371-11375.
16 Hu, J.; Kang, Z.; Li, F.; Huang, X. *Carbon* **2014**, *67*, 221-229.
17 Zhu, G.; He, Z.; Chen, J.; Zhao, J.; Feng, X.; Ma, Y.; Fan, Q.; Wang, L.; Huang, W. *Nanoscale* **2014**, *6*, 1079-1085.
18 Cao, X.; Shi, Y.; Shi, W.; Lu, G.; Huang, X.; Yan, Q.; Zhang, Q.; Zhang, H. *Small* **2011**, *7*, 3163-3168.
19 Chen, Z.; Ren, W.; Gao, L.; Liu, B.; Pei, S.; Cheng, H.-M. *Nat. Mater*. **2011**, *10*, 424-428.
20 Yavari, F.; Chen, Z.; Thomas, A. V.; Ren, W.; Cheng, H.-M.; Koratkar, N. *Sci. Rep*. **2011**, *1*, 166.
21 Pettes, M. T.; Ji, H.; Ruoff, R. S.; Shi, L. *Nano Lett.* **2012**, *12*, 2959-2964.
22 Vickery, J. L.; Patil, A. J.; Mann, S. *Adv. Mater*. **2009**, *21*, 2180-2184.
23 Choi, B. G.; Yang, M.; Hong, W. H.; Choi, J. W.; Huh, Y. S. *ACS Nano* **2012**, *6*, 4020-4028.
24 Huang, X.; Qian, K.; Yang, J.; Zhang, J.; Li, L.; Yu, C.; Zhao, D. *Adv. Mater*. **2012**, *24*, 4419-4423.
25 Xu, Y.; Sheng, K.; Li, C.; Shi, G. *ACS Nano* **2010**, *4*, 4324-4330.
26 Tang, Z.; Shen, S.; Zhuang, J.; Wang, X. *Angew. Chem., Int. Ed*. **2010**, *49*, 4603-4607.
27 Sun, H.; Xu, Z.; Gao, C. *Adv. Mater*. **2013**, *25*, 2554-2560.
28 Niu, Z.; Chen, J.; Hng, H. H.; Ma, J.; Chen, X. *Adv. Mater*. **2012**, *24*, 4144-4150.
29 Sheng, K.; Sun, Y.; Li, C.; Yuan, W.; Shi, G. *Sci. Rep*. **2012**, *2*, 247.
30 Chen, K.; Chen, L.; Chen, Y.; Bai, H.; Li, L. *J. Mater. Chem.* **2012**, *22*, 20968-20976.
31 Yoo, J. J.; Balakrishnan, K.; Huang, J.; Meunier, V.; Sumpter, B. G.; Srivastava, A.; Conway, M.; Mohana Reddy, A. L.; Yu, J.; Vajtai, R.; Ajayan, P. M. *Nano Lett*. **2011**, *11*, 1423-1427.
32 Xu, Z.; Gao, C. *Nat. Commun*. **2011**, *2*, 571.
33 Xu, Z.; Gao, C. *Acc. Chem. Res*. **2014**, *47*, 1267-1276.
34 Xu, Z.; Gao, C. *ACS Nano* **2011**, 5, 2908-2915.
35 Liu, Z.; Li, Z.; Xu, Z.; Xia, Z.; Hu, X.; Kou, L.; Peng, L.; Wei, Y.; Gao, C. *Chem. Mater*. **2014**. dx.doi.org/10.1021/cm5033089
36 Kou, L.; Huang, T.; Zheng, B.; Han, Y.; Zhao, X.; Gopalsamy, K.; Sun, H.; Gao, C. *Nat. Commun*. **2014**, *5*, 3754.
37 Xu, Z.; Sun, H.; Zhao, X.; Gao, C. *Adv. Mater*. **2013**, *25*, 188-193.
38 Kou, L.; Gao, C. *Nanoscale* **2011**, *3*, 519-528.
39 He, H.; Gao, C. *Chem. Mater*. **2010**, *22*, 5054-5064.
40 Yan, J.; Wang, Q.; Wei, T.; Jiang, L.; Zhang, M.; Jing, X.; Fan, Z. *ACS Nano* **2014**, *8*, 4720-4729.
41 Zhu, Y.; Murali, S.; Stoller, M. D.; Ganesh, K. J.; Cai, W.; Ferreira, P. J.; Pirkle, A.; Wallace, R. M.; Cychosz, K. A.; Thommes, M.; Su, D.; Stach, E. A.; Ruoff, R. S. *Science* **2011**, *332*, 1537-1541.
42 Zhang, L.; Shi, G. *J. Phys. Chem. C* **2011**, *115*, 17206-17212.
43 Wang, Y.; Shi, Z.; Huang, Y.; Ma, Y.; Wang, C.; Chen, M.; Chen, Y. *J. Phys. Chem. C* **2009**, *113*, 13103-13107.
44 McAllister, M. J.; Li, J.-L.; Adamson, D. H.; Schniepp, H. C.; Abdala, A. A.; Liu, J.; Herrera-Alonso, M.; Milius, D. L.; Car, R.; Prud'homme, R. K.; Aksay, I. A. *Chem. Mater*. **2007**, *19*, 4396-4404.
45 Branchaud, B. P. *J. Am. Chem. Soc*. **2005**, *127*, 14117-14118.
46 Park, S.; Hu, Y.; Hwang, J. O.; Lee, E.-S.; Casabianca, L. B.; Cai, W.; Potts, J. R.; Ha, H.-W.; Chen, S.; Oh, J.; Kim, S. O.; Kim, Y.-H.; Ishii, Y.; Ruoff, R. S. *Nat. Commun*. **2012**, *3*, 638.